applied sciences

MDPI

Article

Study on Actuator Line Modeling of Two NREL 5-MW Wind Turbine Wakes

Ziying Yu [1], Xing Zheng [1,*] and Qingwei Ma [1,2]

[1] College of Shipbuilding Engineering, Harbin Engineering University, Harbin 150001, China; djwnfbnx@foxmail.com (Z.Y.); q.ma@city.ac.uk (Q.M.)

[2] School of Mathematics, Computer Sciences & Engineering, City, University of London, London EC1V 0HB, UK

* Correspondence: zhengxing@hrbeu.edu.cn; Tel.: +86-451-8256-8147

Received: 8 February 2018; Accepted: 9 March 2018; Published: 13 March 2018

Abstract: The wind turbine wakes impact the efficiency and lifespan of the wind farm. Therefore, to improve the wind plant performance, research on wind plant control is essential. The actuator line model (ALM) is proposed to simulate the wind turbine efficiently. This research investigates the National Renewable Energy Laboratory 5 Million Watts (NREL 5-MW) wind turbine wakes with Open Field Operation and Manipulation (OpenFOAM) using ALM. Firstly, a single NREL 5-MW turbine is simulated. The comparison of the power and thrust with Fatigue, Aerodynamics, Structures, and Turbulence (FAST) shows a good agreement below the rated wind speed. The information relating to wind turbine wakes is given in detail. The top working status is proved at the wind speed of 8 m/s and the downstream distance of more than 5 rotor diameters (5*D*). Secondly, another case with two NREL 5-MW wind turbines aligned is also carried out, in which 7*D* is validated as the optimum distance between the two turbines. The result also shows that the upstream wind turbine has an obvious influence on the downstream one.

Keywords: wind turbine wakes; ALM; NREL 5-MW; OpenFOAM; two wind turbines

1. Introduction

The flow passing through a wind turbine always makes the performance of its downstream wind turbine less efficient than that which was designed. This influence can decrease 10–20% of the production of the total wind farm [1] and increase 5–15% of the loading on the wind turbine blades [2,3]. So it is significant to design the wind turbine by analyzing the wake-induced power and fatigue. Generally speaking, these wakes are very complicated and difficult to reproduce.

There are usually two methods employed to calculate the performance and loading of the wind turbines. One is the Blade-Element/Momentum (BEM) theory [4,5]. It is simple and computationally efficient, but needs to introduce some three-dimensional corrections, tip loss, dynamic stall, etc., to approximate the true situation. The other is the computational fluid dynamics (CFD) method. It can solve the physical problem accurately but always runs on a computer with consuming time. Despite this, many related researches on the simulation of the wind turbine have been documented by using Computational Fluid Dynamics (CFD) [6–8]. Besides, there also exist some other models that can always be used, including the actuator disc model [9], the actuator line model (ALM) [10], and the actuator surface model [11]. In these actuator models, the body forces are distributed in the flow field. Initially, the actuator disc model was used in the wind turbine far wake simulation. However, it could not reproduce the tip vortex system accurately [12]. Then, ALM was introduced by Shen and Sørensen [10] to overcome this difficulty, where the body forces were distributed radially along the blades and added to the three dimensional Navier-Stokes equations as the source item. Moreover, ALM is also an effective technique for predicting the loading on the blades with only simple structured

grids, which has been proved by Troldborg [12]. Recently, Meng et al. [13] firstly proposed the concept of the elastic actuator line (EAL), which combines ALM and a finite difference structural model. In the EAL model, the elastic blades are incorporated into ALM and its simulation results are closer to the reality. Nevertheless, there still exists some limitations in EAL and this needs further study for the improvement of the theory of the actuator line.

For quite a while, most models using ALM were realized by the in-house code, and there is very little commercial ALM software before 2013. Then, the National Renewable Energy Laboratory (NREL) in America developed a CFD tool called Simulator for Off/Onshore Wind Farm Applications (SOWFA) [14], which coupled the OpenFOAM [15] and FAST [16]. It contains the ALM and the atmospheric boundary layer (ABL) model. Fleming et al. [17,18] used it to simulate the wake of the two-turbine case and the result was accurate enough for a practical purpose. Recently, Bachant et al. [19] have developed a library named turbinesFoam, which uses ALM to simulate the hydrokinetics of wind and marine turbines in OpenFOAM. Its interpolation, Gaussian projection, and vector rotation functions are all adapted from NREL's SOWFA.

In this paper, the contents of each section are organized as follows: Firstly, the concept of ALM is reviewed and the tip loss corrections [20] for the computations are given in brief. Then, an uncertainty analysis is carried out through a typical airfoil. After this, the single NREL 5-MW wind turbine case is used as the computational validation. Finally, the influence of the downstream wind turbine rotor speed and the separation distance between the two wind turbines on the whole system performance is examined. Moreover, the velocity fields in the wake flow are also analyzed. Considering the size of the domain, turbinesFoam is used to implement the computational task. The main reference data and the airfoil data can be found from the report of NREL [21].

2. Theoretical Model

2.1. Basic Theory of Actuator Line

The Navier-Stokes (N-S) equations and the actuator line concept are combined as follows:

$$\frac{\partial V}{\partial t} + V \cdot \nabla V = -\frac{1}{\rho}\nabla p + v\nabla^2 V + f_\varepsilon \tag{1}$$

$$\nabla \cdot V = 0 \tag{2}$$

where V is the wind speed; t is the time; ρ is the air density, and $\rho = 1.225\ \mathrm{kg/m^3}$ in this paper; p is the pressure; v is the kinematic viscosity, and it is set as $1.5 \times 10^{-5}\ \mathrm{m^2/s}$; and f_ε is the loading on the blade as the body force that is added into the momentum equations.

The body forces are located along the actuator lines, which represent the blades, as shown in Figure 1, and they are calculated by the blade-element theory with two-dimensional airfoil data. The lift and drag acting on the blade element are, respectively:

$$L = \frac{1}{2}C_l(\alpha)\rho {U_{rel}}^2 c dr \tag{3}$$

$$D = \frac{1}{2}C_d(\alpha)\rho {U_{rel}}^2 c dr \tag{4}$$

where L and D represent the lift and drag, respectively; $C_l(\alpha)$ and $C_d(\alpha)$ are the lift and drag coefficients, correspondingly; α is the local angle of attack; U_{rel} is the local velocity relative to the blade; c is the chord length; and dr is the thickness of the blade element. Figure 2 shows that local velocity relative to the blade can be calculated by:

$$U_{rel} = \sqrt{{U_z}^2 + (\Omega r - U_\theta)^2} \tag{5}$$

where U_z and U_θ are the axial and tangential velocity, respectively; Ω is the rotating angular velocity; and r is the rotating radius. Additionally, the angle of attack is:

$$\alpha = \phi - \gamma \tag{6}$$

where ϕ is the angle of the inflow and γ is the local pitch angle. Therefore, the force per spanwise unit length is:

$$f = (L, D) = \frac{1}{2}\rho {U_{rel}}^2 c(C_l \vec{e_L} + C_d \vec{e_D}) \tag{7}$$

where $\vec{e_L}$ and $\vec{e_D}$ are the unit direction vectors of L and D, respectively.

As the source term in Equation (1) is given in the form of the curl of the load, it acts as a singular vorticity source along the rotor blades. To avoid singularity, a constant ε is added to adjust the strength of the regularization kernel function, and one form can be shown as:

$$\eta_\varepsilon(d) = \frac{1}{\varepsilon^3 \pi^{3/2}} \exp[-(\frac{d_i}{\varepsilon})^2] \tag{8}$$

where d_i is the distance between the measured point (x_i, y_i, z_i) and initial force points (x, y, z) on the blade. η_ε is the kernel function between the measured and initial force points, which is quite similar to the kernel function used in Smoothed Particle Hydrodynamics (SPH) [22]. Finally, f_ε on the nearby mesh can be calculated by:

$$f_\varepsilon(x, y, z, t) = f \otimes \eta_\varepsilon = \sum_{j=1}^{N} f(x_i, y_i, z_i, t) \frac{1}{\varepsilon^3 \pi^{3/2}} \exp[-(\frac{d_i}{\varepsilon})^2] \tag{9}$$

where N is the number of neighbouring blade sections. It means that the discreted force on each blade section can be interpolated to the neigbouring mesh nodes smoothly. More details on the solution of Equation (9) can be referred to in [10]. To add the tower and hub effect into ALM, these will be achieved by following a similar technology.

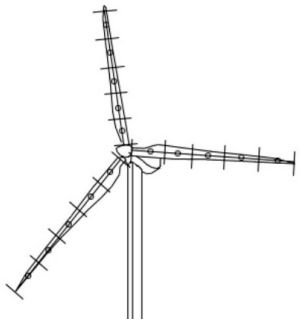

Figure 1. Blades represented by actuator lines.

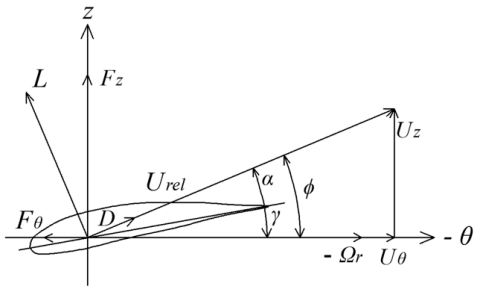

Figure 2. Cross-sectional airfoil element.

2.2. Tip Loss Correction Model

In order to simulate a real wind turbine, the tip loss effects must be introduced. The tip loss correction model is used here to take into account the difference between the ALM and the actual blades, where the velocity should always be zero at the tip. This always makes the actual loading on the blades different to the loading we obtain. This concept was introduced by Prandtl, and refined by many scholars. In the present research, the Prandtl-Glauert model and Shen model [20] are used. The Prandtl-Glauert tip loss function is introduced firstly by,

$$F_{tip} = \frac{2}{\pi}\arccos[\exp(-\frac{B(R-r)}{2r\sin\phi})] \tag{10}$$

where B is the number of the blades; R is the radius of the blades; r is the distance between the blade-element location and the root of the blade; and ϕ is the angle between the local relative velocity and the rotor plane. Then, Shen improved the function into:

$$F_{tip} = \frac{2}{\pi}\arccos[\exp(-g\frac{B(R-r)}{2r\sin\phi})] \tag{11}$$

where g is a coefficient that depends on the tip speed ratio, numbers of blades, pitch setting, and chord distribution, etc. Furthermore, he also assumed g as the following form:

$$g = \exp[-c_1(B\lambda - c_2)] + 0.1 \tag{12}$$

where c_1 and c_2 are the two coefficients determined from the experimental data. They are set as c_1 = 0.125 and c_2 = 21 in this paper.

2.3. Refrence Data of NREL 5-MW

The NREL 5-MW wind turbine is a conventional three-blade upwind variable-speed variable-blade-pitch-to-feather-controlled turbine. Its rotor diameter is about 126 m and the hub height is nearly 90 m. The rated wind speed is 11.4 m/s. Under the rated wind speed, the rotor speed is 12.1 rpm and the power is 5 MW. The structure of the blades used in ALM is shown in Table 1. Additionally, the radius of the tower top is 3 m and it is linearly distributed along the tower.

Table 1. Distributed blade structural and aerodynamic properties.

Radius (m)	Chord (m)	Chord Mount	Airfoil Properties
0.000	3.542	0.25	-
1.367	3.542	0.249	Cylinder1
4.100	3.854	0.222	Cylinder1
6.833	4.167	0.188	Cylinder1
10.250	4.557	0.146	Cylinder2
14.350	4.652	0.125	DU [1] 40
18.450	4.458	0.125	DU35
22.550	4.249	0.125	DU35
26.650	4.007	0.125	DU30
30.750	3.748	0.125	DU25
34.850	3.502	0.125	DU25
38.950	3.256	0.125	DU21
43.050	3.010	0.125	DU21
47.150	2.764	0.125	NACA [2] 64
51.250	2.518	0.125	NACA64
54.667	2.313	0.125	NACA64
57.400	2.086	0.125	NACA64
60.133	1.419	0.125	NACA64
61.500	0.961	0.125	NACA64

[1] Delft University; [2] National Advisory Committee for Aeronautics.

3. Uncertainty Analysis of a Typical Airfoil Flow

3.1. Numerical Model

Flow occurs around a NACA 0012 airfoil at Reynolds number based on the airfoil chord c, incoming velocity V_∞, and fluid kinematic viscosity ν of $Re = 6 \times 10^6$ at two angles of attack β, $\beta = 4^\circ$ and 10°. For each attack angle, there are nine geometrically similar grids with available refinement based on OpenFOAM. The domain for the calculation of the flow over around the NACA 0012 airfoils is shown in Figure 3, where c is the chord of the airfoil. The inlet is a semicircle with $r = 12c$ and the outlet is placed $13c$ downstream of the trailing edge of the airfoil. The external boundary is located approximately $12c$ away from the airfoil. The Reynolds number based on the velocity of the incoming flow V_∞, chord of the foil c.

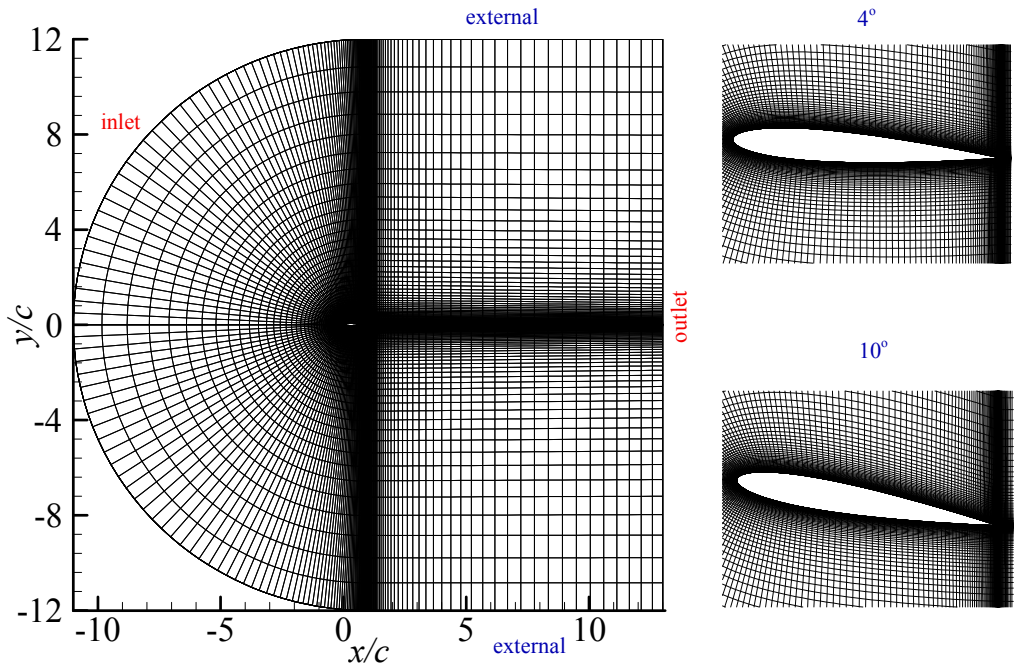

Figure 3. Simulation domain of NACA0012. NACA: National Advisory Committee for Aeronautics.

Distribution of grid nodes is defined by the one-sided stretching functions proposed by Vinokur [23]. For the sake of completeness, the largest, average, and smallest dimensionless distance of the near-wall cell centre to the airfoil surface are included in the file that contains the lift (C_L) and drag (C_d) coefficients of the airfoil. u_τ is the friction velocity defined by $u_\tau = \sqrt{\frac{\tau_\omega}{\rho}}$, where τ_ω is the shear-stress at the wall and ρ is the fluid density. The grid refinement ratio r_i may be obtained from the total number of cells N_{cells}:

$$r_i = \frac{h_i}{h_1} = \sqrt{\frac{(N_{cells})_1}{(N_{cells})_i}} \tag{13}$$

The number of cells is independent of the angle of attack β and the values of N_{cells} and r_i are given in Table 2.

Table 2. Mesh information of airfoil simulation.

r_i	N_{cells}
	4° and 10°
1.000	929,280
1.143	711,480
1.333	522,720
1.600	363,000
2.000	232,320
2.286	177,870
2.667	130,680
3.200	90,750
4.000	58,080

3.2. Uncertainty Analysis

There are various existing verification methods for solution verification, and it is a common practice to retain only the first term of the Richardson extrapolation and assume that the solutions are in the asymptotic range, which leads to a grid-triplet study. The Grid Convergence Index (GCI) derived by Roache [24] can be used to estimate the uncertainties due to grid-spacing and time-step errors and is widely used and recommended by American Society of Mechanical Engineers (ASME) [25] and American Institute of Aeronautics and Astronautics (AIAA) [26]. The other two common verification methods in ship hydrodynamics are Factor of Safety methods (FS) developed by Xing and Stern [27] and Least Squared Root methods (LSR) introduced by Eça [28]. The Least Squared Root methods (LSR) are applied in this paper.

Nowadays, the most common verification methods in CFD are based on Richardson extrapolation. Then, discrete solutions φ are assumed to:

$$\phi_i = \phi_0 + \alpha h_i^p \tag{14}$$

In which φ_0 is the exact value, p is the order of convergence, and α is a constant.

The LSR is based on power series expansions that neglect high-order terms and assume that φ has at least second-order finite derivatives. It is also assumed that the lowest-order schemes used in the discretization are second or first-order accurate. The present subsection will show the procedure for numerical uncertainty estimation with the latest LSR method in the following:

(1) Determination of ε_ϕ

Solve the non-linear equations, Equation (15), in the least-squares sense with and without weights to obtain δ_{RE} ($\delta_{RE} = \phi_i - \phi_0$), p, and the standard deviations of the two fits σ.

$$\begin{cases} \phi_0 = \sum\limits_{i=1}^{n_g} w_i\phi_i - \alpha \sum\limits_{i=1}^{n_g} w_i h_i^p \\ \alpha = \dfrac{\sum\limits_{i=1}^{n_g} w_i\phi_i h_i^p - \left(\sum\limits_{i=1}^{n_g} w_i\phi_i\right)\left(\sum\limits_{i=1}^{n_g} w_i h_i^p\right)}{\sum\limits_{i=1}^{n_g} w_i h_i^{2p} - \left(\sum\limits_{i=1}^{n_g} w_i h_i^p\right)\left(\sum\limits_{i=1}^{n_g} w_i h_i^p\right)} \\ \sum\limits_{i=1}^{n_g} w_i\phi_i h_i^p \log(h_i) - \phi_0 \sum\limits_{i=1}^{n_g} w_i h_i^p \log(h_i) - \alpha \sum\limits_{i=1}^{n_g} w_i h_i^{2p} \log(h_i) = 0 \end{cases} \tag{15}$$

where w is the weighted number, $w_i = 1$, and $nw_i = 1$ in the non-weighted approach. For the weighted approach, $w_i = \dfrac{1/h_i}{\sum\limits_{i=1}^{ng} 1/h_i}$ and n_g is the grid number, which is supposed to be at least 4.

The standard deviation is given by:

$$\sigma_{RE} = \sqrt{\frac{\sum_{i=1}^{n_g} nw_i\left(\phi_i - \left(\phi_0 + \alpha h_i^p\right)\right)^2}{n_g - 3}} \tag{16}$$

If any of the fits exhibit $0.5 \leq p \leq 2$, $\varepsilon_\phi = \delta_{RE}$. If both fits exhibit $0.5 \leq p \leq 2$, the value of δ_{RE} selected corresponds to the fit with the smallest standard deviation.

If the observed order of grid convergence is $p > 2$, solve the non-linear equations, Equations (17)–(19), in the least-squares sense with and without weights and determine the standard deviations of the six fits σ. ε_ϕ is obtained from the fit that exhibits the smallest standard deviation.

$$\begin{bmatrix} 1 & \sum_{i=1}^{n_g} w_i h_i \\ \sum_{i=1}^{n_g} w_i h_i & \sum_{i=1}^{n_g} w_i h_i^2 \end{bmatrix} \begin{bmatrix} \phi_0 \\ \alpha \end{bmatrix} = \begin{bmatrix} \sum_{i=1}^{n_g} w_i \phi_i \\ \sum_{i=1}^{n_g} w_i \phi_i h_i \end{bmatrix} \tag{17}$$

$$\begin{bmatrix} 1 & \sum_{i=1}^{n_g} w_i h_i^2 \\ \sum_{i=1}^{n_g} w_i h_i^2 & \sum_{i=1}^{n_g} w_i h_i^4 \end{bmatrix} \begin{bmatrix} \phi_0 \\ \alpha \end{bmatrix} = \begin{bmatrix} \sum_{i=1}^{n_g} w_i \phi_i \\ \sum_{i=1}^{n_g} w_i \phi_i h_i^2 \end{bmatrix} \tag{18}$$

$$\begin{bmatrix} 1 & \sum_{i=1}^{n_g} w_i h_i & \sum_{i=1}^{n_g} w_i h_i^2 \\ \sum_{i=1}^{n_g} w_i h_i & \sum_{i=1}^{n_g} w_i h_i^2 & \sum_{i=1}^{n_g} w_i h_i^3 \\ \sum_{i=1}^{n_g} w_i h_i^2 & \sum_{i=1}^{n_g} w_i h_i^3 & \sum_{i=1}^{n_g} w_i h_i^4 \end{bmatrix} \begin{bmatrix} \phi_0 \\ \alpha_1 \\ \alpha_2 \end{bmatrix} = \begin{bmatrix} \sum_{i=1}^{n_g} w_i \phi_i \\ \sum_{i=1}^{n_g} w_i \phi_i h_i \\ \sum_{i=1}^{n_g} w_i \phi_i h_i^2 \end{bmatrix} \tag{19}$$

The standard deviations are given by Equations (20)–(22), respectively.

$$\sigma_1 = \sqrt{\frac{\sum_{i=1}^{n_g} nw_i(\phi_i - (\phi_0 + \alpha h_i))^2}{n_g - 2}} \tag{20}$$

$$\sigma_2 = \sqrt{\frac{\sum_{i=1}^{n_g} nw_i\left(\phi_i - \left(\phi_0 + \alpha h_i^2\right)\right)^2}{n_g - 2}} \tag{21}$$

$$\sigma_{12} = \sqrt{\frac{\sum_{i=1}^{n_g} nw_i\left(\phi_i - \left(\phi_0 + \alpha_1 h_i + \alpha_2 h_i^2\right)\right)^2}{n_g - 3}} \tag{22}$$

(2) Determine the following data range parameter to assess the quality of the fit used to obtain the error estimate ε_ϕ

$$\Delta_\phi = \frac{(\phi_i)_{\max} - (\phi_i)_{\min}}{n_g - 1} \tag{23}$$

(3) Determine the safety factor

If $0.5 \leq p < 2.1$ and $\sigma < \Delta_\phi$, $F_s = 1.25$; otherwise, $F_s = 3$.

(4) Obtain the uncertainty

For $\sigma < \Delta_\phi$:

$$U_\phi(\phi_i) = F_S \varepsilon_\phi(\phi_i) + \sigma + \left|\phi_i - \phi_{fit}\right| \tag{24}$$

For $\sigma \geq \Delta_\phi$:

$$U_\phi(\phi_i) = 3\frac{\sigma}{\Delta_\phi}\left(\varepsilon_\phi(\phi_i) + \sigma + \left|\phi_i - \phi_{fit}\right|\right) \tag{25}$$

The lift (C_L) and drag (C_d) coefficients with different attack angles are shown in Table 3.

Table 3. Lift (C_L) and drag (C_d) coefficients with different attack angles.

r_i	4°		10°	
	C_d	C_L	C_d	C_L
4.000	9.599×10^{-3}	4.342×10^{-1}	1.583×10^{-2}	1.058
3.200	9.484×10^{-3}	4.346×10^{-1}	1.558×10^{-2}	1.060
2.667	9.325×10^{-3}	4.353×10^{-1}	1.526×10^{-2}	1.062
2.286	9.326×10^{-3}	4.352×10^{-1}	1.530×10^{-2}	1.061
2.000	9.348×10^{-3}	4.351×10^{-1}	1.535×10^{-2}	1.061
1.600	9.263×10^{-3}	4.353×10^{-1}	1.532×10^{-2}	1.062
1.333	9.224×10^{-3}	4.357×10^{-1}	1.515×10^{-2}	1.063
1.143	9.226×10^{-3}	4.356×10^{-1}	1.518×10^{-2}	1.063
1.000	9.230×10^{-3}	4.356×10^{-1}	1.518×10^{-2}	1.063

By using the LSR uncertainty estimator which is presented in the previous section, the convergence of lift and drag coefficients with the grid refinement are shown in Figures 4 and 5, respectively. The lift coefficient is nearly zero when the angle of attack is zero, so these lift coefficients are not analyzed. The error bars for the mesh ratio equal to 1.0, 2.0, and 4.0 are also included in those figures. Then, Table 4 displays the uncertainty of the lift and drag coefficient with the grid refinement for different angle of attacks. It is clear that the error and uncertainty are reduced with the mesh refinement. Finally, we can bound the exact value (ϕ_{exact}) and the interval is:

$$\phi_i - U_{\phi_i} \leq \phi_{exact} \leq \phi_i + U_{\phi_i} \tag{26}$$

Table 5 shows the interval of the exact lift and drag coefficient with the grid refinement for different angle of attacks. Figure 6 shows the uncertainty of the drag and lift coefficient with the grid refinement for different attack angles. Considering the experiment results of NACA 0012 by Ladson [29] and McCroskey [30], the results are well bounded by the OpenFOAM uncertainty interval.

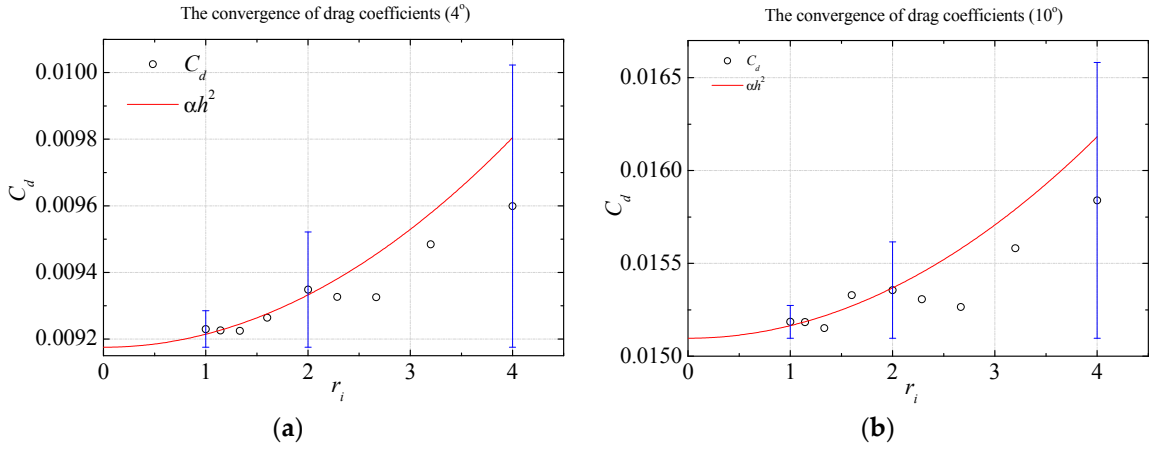

Figure 4. Convergence of the drag coefficient with the grid refinement (Fits obtained from the data with $1 \leq r_i \leq 2$) by different attack angles: (**a**) 4°; (**b**) 10°. Blue line: Error bar.

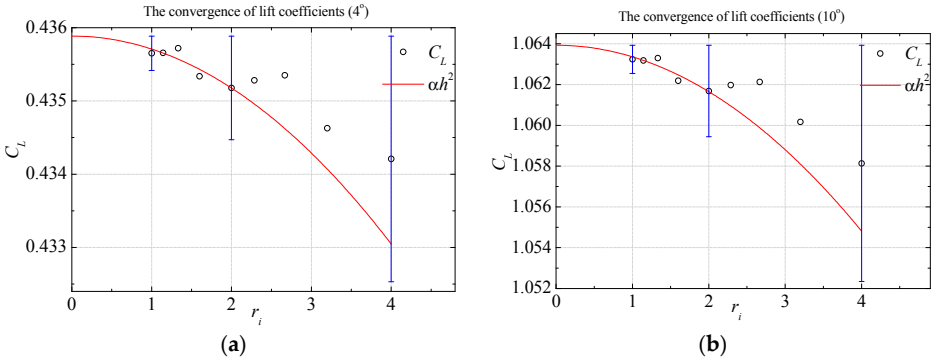

Figure 5. Convergence of the lift coefficient with the grid refinement (Fits obtained from the data with $1 \leq r_i \leq 2$) by different attack angles: (**a**) 4°; (**b**) 10°. Blue line: Error bar.

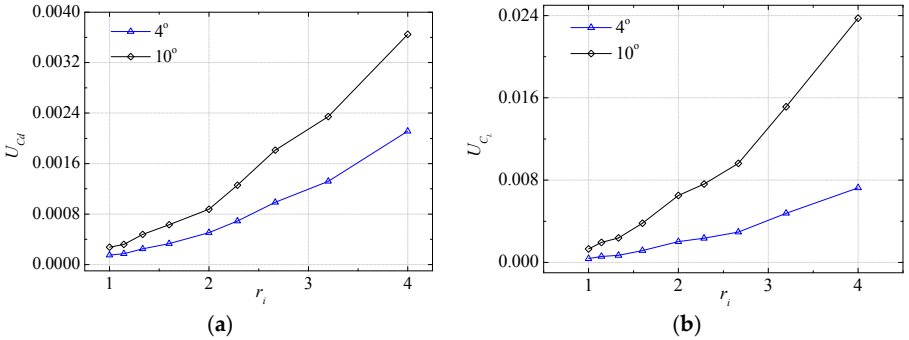

Figure 6. Uncertainty of the drag and lift coefficient with the grid refinement for different attack angles: (**a**) U_{CL}; (**b**) U_{Cd}.

Table 4. The uncertainty of lift and drag coefficient with the grid refinement for different attack angles.

r_i	4°		10°	
	U_{Cd}	U_{CL}	U_{Cd}	U_{CL}
1.000	1.519×10^{-4}	3.684×10^{-4}	2.751×10^{-4}	1.308×10^{-3}
1.143	1.733×10^{-4}	5.861×10^{-4}	3.189×10^{-4}	1.946×10^{-3}
1.333	2.486×10^{-4}	6.900×10^{-4}	4.784×10^{-4}	2.376×10^{-3}
1.600	3.327×10^{-4}	1.163×10^{-3}	6.305×10^{-4}	3.812×10^{-3}
2.000	5.065×10^{-4}	2.020×10^{-3}	8.771×10^{-4}	6.518×10^{-3}
2.286	6.895×10^{-4}	2.350×10^{-3}	1.258×10^{-3}	7.625×10^{-3}
2.667	9.874×10^{-4}	2.952×10^{-3}	1.812×10^{-3}	9.624×10^{-3}
3.200	1.320×10^{-3}	4.785×10^{-3}	2.344×10^{-3}	1.513×10^{-3}
4.000	2.113×10^{-3}	7.247×10^{-3}	3.649×10^{-3}	2.373×10^{-3}

Table 5. Range of exact lift and drag coefficient with the grid refinement for different attack angles.

r_i	4°				10°			
	C_d		C_L		C_d		C_L	
	$C_d - U_{Cd}$	$C_d + U_{Cd}$	$C_L - U_{CL}$	$C_L + U_{CL}$	$C_d - U_{Cd}$	$C_d + U_{Cd}$	$C_L - U_{CL}$	$C_L + U_{CL}$
1.000	9.078×10^{-3}	9.382×10^{-3}	4.352×10^{-1}	4.360×10^{-1}	1.491×10^{-2}	1.546×10^{-2}	1.061	1.064
1.143	9.052×10^{-3}	9.399×10^{-3}	4.350×10^{-1}	4.362×10^{-1}	1.486×10^{-2}	1.550×10^{-2}	1.061	1.065
1.333	8.976×10^{-3}	9.473×10^{-3}	4.350×10^{-1}	4.364×10^{-1}	1.467×10^{-2}	1.563×10^{-2}	1.060	1.065
1.600	8.931×10^{-3}	9.596×10^{-3}	4.341×10^{-1}	4.365×10^{-1}	1.469×10^{-2}	1.595×10^{-2}	1.058	1.066
2.000	8.841×10^{-3}	9.855×10^{-3}	4.331×10^{-1}	4.371×10^{-1}	1.447×10^{-2}	1.623×10^{-2}	1.055	1.068
2.286	8.637×10^{-3}	1.001×10^{-2}	4.329×10^{-1}	4.376×10^{-1}	1.404×10^{-2}	1.656×10^{-2}	1.054	1.069
2.667	8.338×10^{-3}	1.031×10^{-2}	4.323×10^{-1}	4.383×10^{-1}	1.345×10^{-2}	1.707×10^{-2}	1.052	1.071
3.200	8.163×10^{-3}	1.080×10^{-2}	4.298×10^{-1}	4.394×10^{-1}	1.323×10^{-2}	1.792×10^{-2}	1.045	1.075
4.000	7.485×10^{-3}	1.171×10^{-2}	4.269×10^{-1}	4.414×10^{-1}	1.219×10^{-2}	1.948×10^{-2}	1.034	1.081

4. A Single NREL 5-MW Turbine Case

In this section, a single NREL 5-MW wind turbine case is built to identify the accuracy of the model. Additionally, there are three cases with different representative wind speeds to find the reason why the wind speed is 8 m/s in some studies. These wind speeds are set as 11.4 m/s, 8 m/s, and 5 m/s, respectively. The wind turbine obtains the rated status at the wind speed of 11.4 m/s, and the tip speed ratio is 7. When the wind speed is 8 m/s, the power coefficient is up to the maximum and the corresponding tip speed ratio is 7.55. Compared with the two cases above, the last case is set, in which the wind speed is used as 5 m/s.

4.1. Numerical Model

The wind turbine is placed in a domain of 1890 m × 1260 m × 468 m. Details are shown in Figure 7, which shows that the mesh is refined by three steps in a rectangular region. The size of the cell outside the refinement zone is approximately 24 m; therefore, the inner zone mesh size is nearly 3 m. In addition, the regions behind the blade tip and root are important for ascertaining an accurate wake structure, so these parts are refined by the smaller mesh, which is indicated in Figure 8. In order to reduce the artificial reflections and oscillations, the refined ratio is set to 2 and three levels are adopted to avoid a large refinement ratio. Meshes are generated by blockMesh and snappyHexMesh in OpenFOAM. The wind turbine and the tower are set by topoSet.

The wind flow is steady. The inflow and outflow boundary conditions of U are set by the fixedValue and inletOutlet, respectively, and zeroGradient and fixedValue are used correspondingly for the pressure p. All others are defined as the slip boundary. The Reynolds-averaged Navier-Stokes (RANS) equations using the shear stress transport (SST) $k-\omega$ turbulence model are considered in this model. The pressure-velocity coupling solver application uses the combined the Pressure-Implicit split-operator (PISO) and the semi-implicit Method for Pressure-Linked Equations (SIMPLE) algorithms, which be can be abbrivated as PIMPLE. The number of times that the algorithm solves the pressure equation and momentum corrector in each step is 2. The solver for p is GAMG (Generalized geometric-Algebraic Multi-Grid) and for others is smoothSolver, which is a solver that uses a smoother. The numerical schemes are set as Euler for the time marching schemes, which is first-order implicit, with the Gauss liner for the gradient term, and Gauss linerUpwind for the divergence term. Besides, the time-step size is set corresponding to a blade rotation of 1 degree and the data is saved every five time steps. To obtain a relatively stable state, the simulation is calculated for 20 revolutions of the wind turbine. The Glauert model is chosen as the tip loss model.

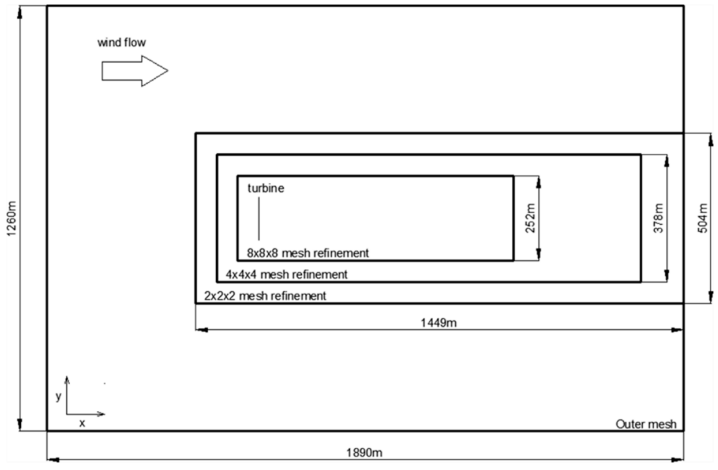

(**a**)

Figure 7. *Cont.*

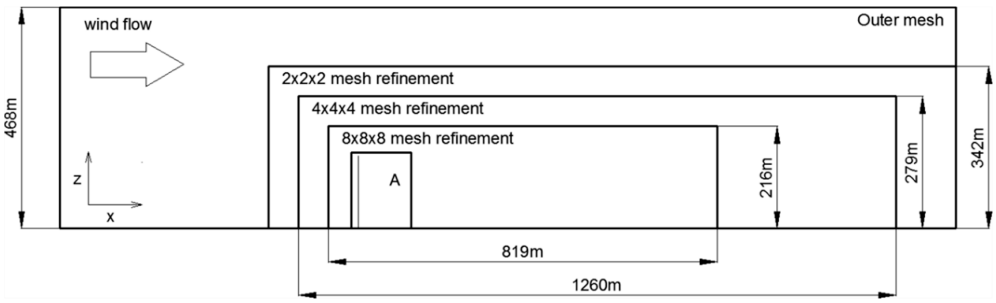

Figure 7. The schematic setup of computational domain: (**a**) Top view; (**b**) Side view.

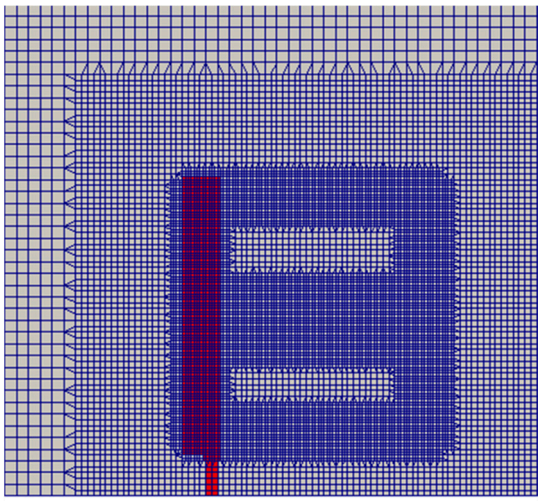

Figure 8. Computational domain mesh of A with refinement. The blue mesh is the fluid domain; the red mesh is the part of wind turbine.

4.2. Validation of Numerical Model

In order to quantify the influence of the mesh quality, a series of computations with variable grid numbers are carried out for U_0 = 11.4 m/s, which are 375,432, 744,792, 2,903,144, and 5,958,336, respectively. As there are no experimental data for a full scale NREL 5-WM wind turbine, it adopts the results of FAST as the benchmark data, which can be referred to in [21]. The simulation time is set 30 s. The power and thrust coefficients are introduced and defined as below:

$$C_p = \frac{P}{0.5\rho U_0^3 \pi R^2} \tag{27}$$

$$C_T = \frac{T}{0.5\rho U_0^2 \pi R^2} \tag{28}$$

where P is the mechanical power; T is the thrust on the blades; and R is the radius of the rotor blade and R = 63 m, ρ = 1.225 kg/m^3. According to reference [21], C_p = 0.4418, C_t = 0.8099 when U_0 = 11.4 m/s. The errors of C_p and C_t of different cell numbers are shown in Table 6. The errors of the power and thrust are compared in Figure 9, which shows that when the numbers of the grid increase, the differences in the power and thrust begin to stabilize. Considering the computational efficiency, the total number of 2,903,144 cells should be high enough to obtain accurate results, considering the errors of C_p and C_t which are 4.858% and 5.981%, respectively.

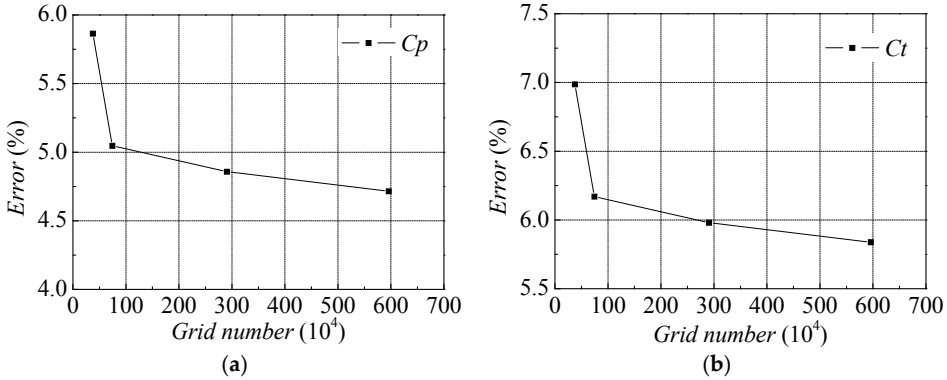

Figure 9. The mesh independence test: (**a**) Error distributions of C_p; (**b**) Error distributions of C_t.

Table 6. The mesh independence test.

Number of Cell	C_p	Error (%)	C_t	Error (%)
375,432	0.4678	5.864	0.8665	6.987
744,792	0.4642	5.047	0.8599	6.170
2,903,144	0.4634	4.858	0.8584	5.981
5,958,336	0.4627	4.715	0.8572	5.838

To examine the accuracy of different wind speeds, the thrust and power are computed and compared with the FAST code [21], which are shown in Figure 10. The results agree with FAST excellently for the wind speeds up to 11.4 m/s. The quantitative values of interest and errors are shown in Table 7.

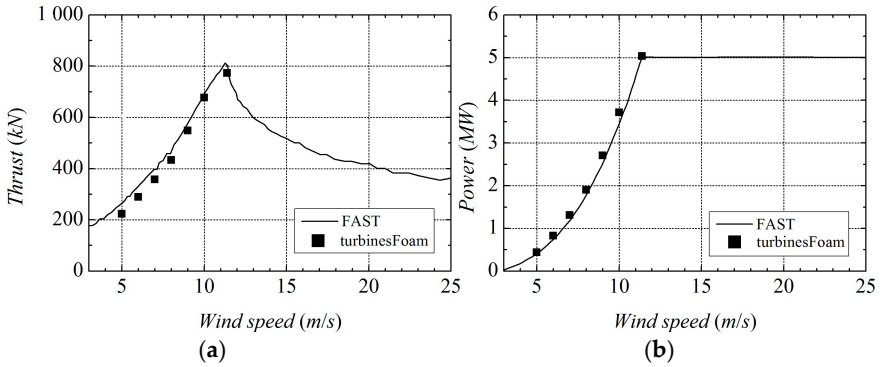

Figure 10. Comparison of the computed power and thrust between FAST and turbinesFoam at different wind speed: (**a**) Thrust; (**b**) Power.

Table 7. Comparison of the computed power and thrust between FAST and turbinesFoam at different wind speeds.

Wind Speed (m/s)	Thrust of TurbinesFoam (kN)	Power of TurbinesFoam (MW)	Thrust of FAST (kN)	Power of FAST (MW)	Thrust Errors (%)	Power Errors (%)
5.0	223.578	0.4400	264.9066	0.4236	15.60	3.88
6.0	288.945	0.8265	331.8101	0.7652	12.92	8.01
7.0	357.735	1.3088	397.2068	1.2240	9.94	6.92
8.0	433.465	1.9026	467.6329	1.8251	7.31	4.25
9.0	548.601	2.7090	577.9532	2.5955	5.08	4.37
10.0	677.285	3.7160	691.1475	3.5587	2.01	4.42
11.4	722.471	5.0363	803.9102	5.000	3.91	0.73

As for the high wind speed, the local Reynolds number of the blades is calculated at the rated wind speed, as defined below:

$$Re = \frac{U_{blade}c}{\nu} \tag{29}$$

where c is the chord length; ν is the air kinematic viscosity; U_{blade} is the local velocity, and can be calculated by $U_{blade} = \sqrt{U_{axial}^2 + (\omega r)^2}$, where U_{axial} is the axial velocity; and ω is the rotating angular velocity. The comparison with the result of the BEM method is depicted in Figure 11. It shows that the local Reynolds number varies in different locations of the blade and the maximum value is near 1.2×10^7, which is far bigger than that given in the reference. Thus, the airfoil data become unreliable for the wind speeds greater than 11.4 m/s. In addition, the size of the wind turbine is so large that the dynamic stall should be considered at the high wind speed. The dynamic stall model is not used in this paper. Additionally, the blades need to adjust their pitch angles and maintain the tip speed ratio to maximize the power output when the wind speed exceeds the rated speed. In summary, large wind speeds are not considered in this work.

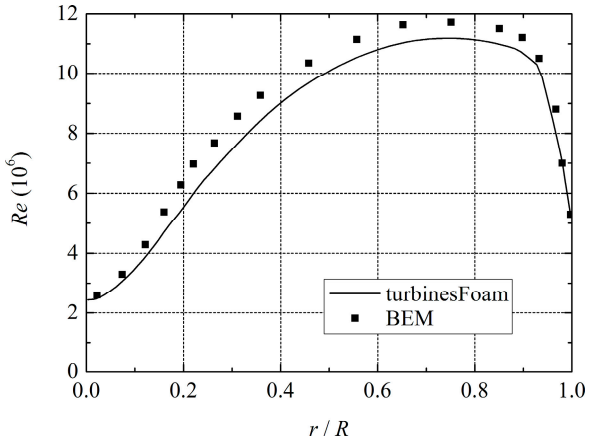

Figure 11. Comparison of the local Reynolds number with the Blade-Element/Momentum (BEM) method.

To validate the effect of the tip loss model, the comparison of the force distributions with and without the tip loss model is given for U_0 = 11.4 m/s (See Figure 12). There is no difference in the middle of the blade, but obvious disagreement is found at the tip if the model of tip loss is not included. Although the discrepancy in the force is small, the residual of power could rise up to 12% (See Table 8). Therefore, it seems to be significant to add the tip loss correction model when using ALM.

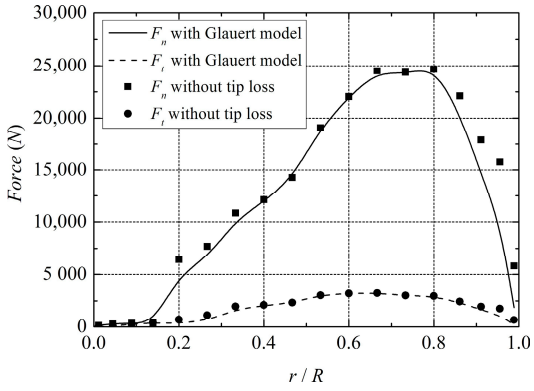

Figure 12. Comparison of radial force distributions with Glauert model and without the tip loss model.

Table 8. Comparison of the power with Glauert model and without the tip loss model.

Methods	Mean Power (MW)	C_p	Difference (%)
Glauert model	5.243	0.4634	4.858
No model	5.600	0.4950	12.018

4.3. Wake Structures

The vortex isosurfaces to illustrate the downstream development of the wake vortices are depicted in Figure 13. The wake vortices are identified by the Q criterion, where Q is adjusted as 0.003 for the three cases. It is shown that the tip and hub vortices are clear behind the rotor. They persist for nearly two turns, diffuse at U_0 = 11.4 m/s, and spread out early when the wind speed decreased, corresponding to the increase in the tip speed ratio. Additionally, they become a continuous vortex sheet at U_0 = 5 m/s.

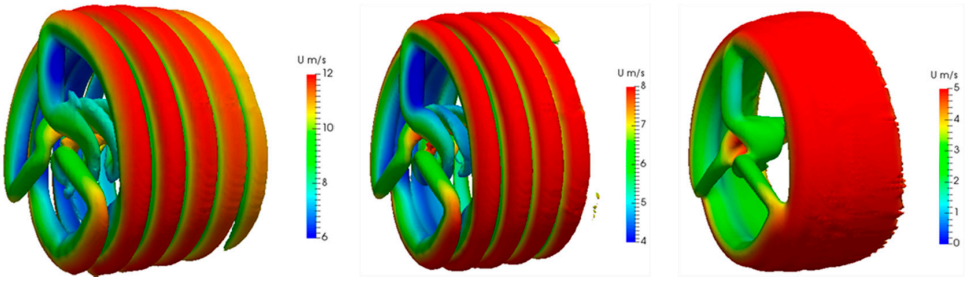

Figure 13. Computed Q field showing the formation of wake structure (Q = 0.003): (**a**) U_0 = 11.4 m/s; (**b**) U_0 = 8 m/s; (**c**) U_0 = 5 m/s.

The axial flow interference factors represent the influence on the performance of the wind turbine and the distribution of the loading on the blades, which can be calculated by:

$$a = 1 - \frac{U_x}{U_0} \tag{30}$$

where U_x is the velocity behind the rotor and U_0 is the wind speed. Figure 14 depicts the radial distributions of averaged axial flow interference factors at different wind speeds. From Figure 14, it can be seen that the curves at the wind speed of 5 m/s and 8 m/s are more generally steady than that of 11.4 m/s, but the values are too large under the wind speed of 5 m/s, which means the loading on the blade is not balanced and the influence on the performance is worse than that under 8 m/s.

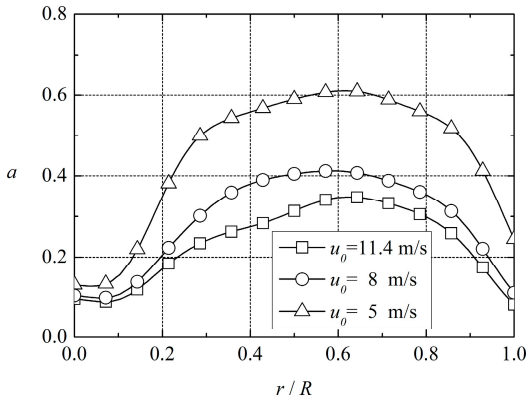

Figure 14. Radial distributions of averaged axial flow interference factors at different wind speeds.

It is common that the wind turbine turns the wind energy into mechanical energy and the reduction of the wind speed is described as the velocity deficit. It depicts the efficiency of the energy transformation and can affect the performance of the downstream wind turbine. The velocity deficit can be seen through the axial velocity distribution, which is simply shown in Figure 15. It is worthwhile to note that the axial velocities have been normalized with the corresponding wind speed and so the normalized velocities at the upstream station are 1. Figure 15 illustrates the curves of the average axial velocity ratio at the hub height. It is easy to see the velocity deficit in the wake and the velocity is recovering with the growing distances. The location of the maximum velocity deficit is around 1D~3D. With the wind speed becoming greater, it moves away from the rotor and becomes higher. That is as indication that the utilization of the wind energy is getting smaller and the rate of the recovery gets slower.

From the above analysis, it can be seen that the utilization of the wind energy and the ratio of the velocity recovery is larger at the low wind speed, but the loading on the blades is so unsteady and the power is too small. It can thus be simply concluded that the wind turbine can work in an oppositely fine status under the wind speed of 8 m/s. In that case, the power coefficient may become coincidently maxima. Thus, it is reasonable that the wind speed has been set as 8 m/s in many documented studies. For further investigation, some representative numerical results are given at 8 m/s in the next section.

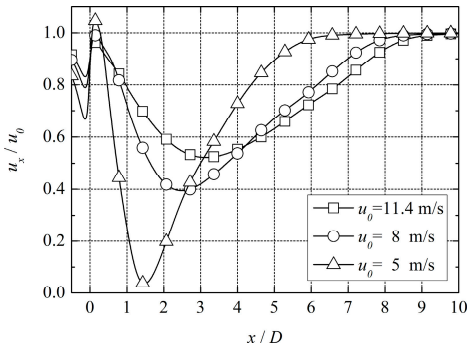

Figure 15. Streamwise profile of the average axial velocity at hub height.

4.4. Results in 8 m/s

The computed power and thrust are 1.9026 MW and 433.47 kN, respectively, and the errors between FAST and these are 4.245% and 5.079%, correspondingly. For more details, the reader can refer to Table 9. Due to the tower's influence on the rotor, the changes in C_p and C_T are not unilateral but periodical (See Figure 16). It can also be seen that the wind turbine can obtain a relatively stable status. Furthermore, the interval between the two extreme points is about 2.2 s. That is when the blades rotate nearly 120 degrees, which is one-third of the cycle of the rotor revolving.

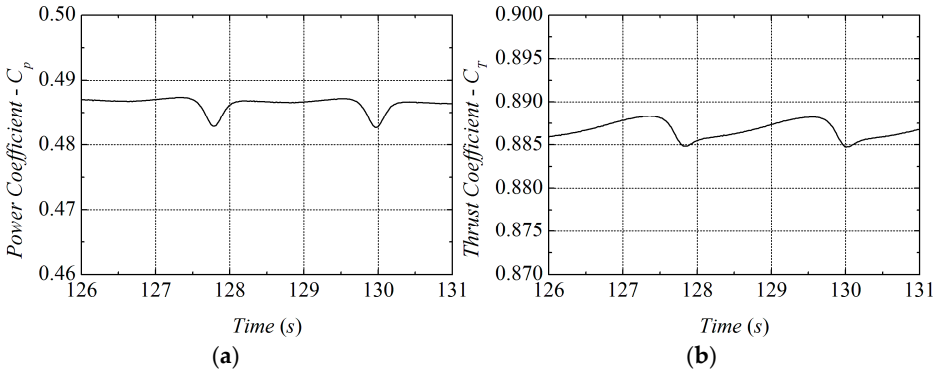

Figure 16. The curves of power and thrust coefficient: (**a**) Power coefficient; (**b**) Thrust coefficient.

Table 9. Comparison of the power and thrust.

Power (MW)	Difference (%)	Thrust (kN)	Error (%)
1.9026	4.245	433.47	5.079

Figure 17 shows the spanwise distribution of the time-averaged normalized axial velocity at the streamwise positions of $-0.5D$, $0.5D$, $1D$, $2D$, $3D$, $5D$, $6D$, $7D$, and $8D$, which represent the development of the velocity in the wake. There is a clear phenomenon of the turbine extracting momentum from the incoming flow when the airflow passes through the wind turbine. That is the velocity deficit. The asymmetrical velocity profile is observed and the velocity value is not 1.0 at $y/D = 0$, when the effects of the tower and the hub are included. The velocity profile changes from a single peak line to double peaks when the wind flows past the rotor, and gradually becomes a single peak again. The double peak line represents that the velocity deficit is large in the middle of the blade and small in the hub, which is an indication that the loading is focused on the middle of the blade. The rate of velocity recovery becomes slower with the increasing distance, which means that the influence of the wake becomes weaker. More details about the wake development can be seen in the research of Mo [31]. It seems that the wake effect is little from $5D$ to $8D$, and further study is presented in the next section.

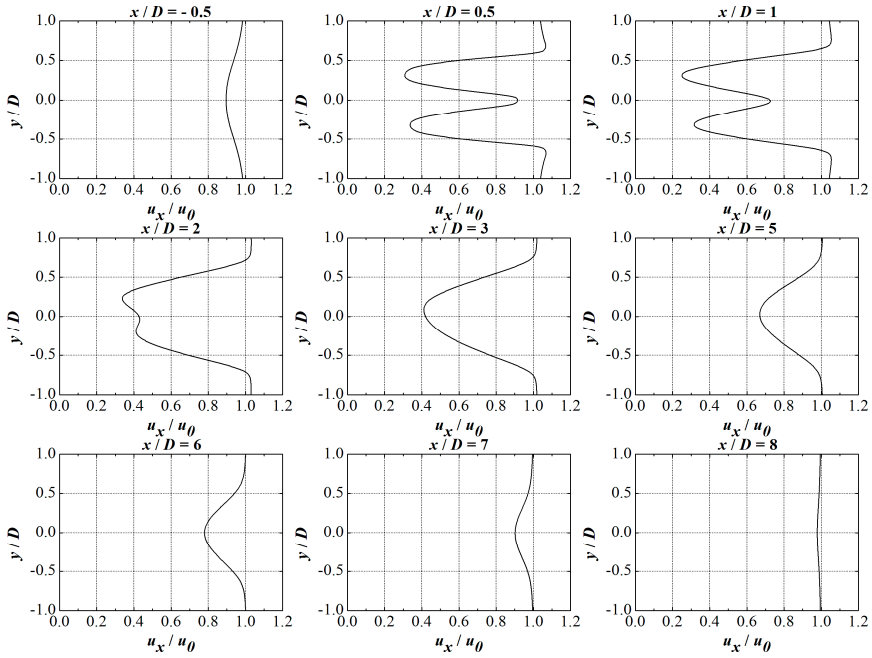

Figure 17. Spanwise distribution of average axial velocity in different streamwise locations.

5. Double NREL 5-MW Wind Turbines Case

In this section, two NREL 5-MW wind turbines that are aligned together are simulated. The upstream wind turbine is set as WT1 and the downstream one is set as WT2. The best tip speed ratio of WT2 is calculated and the best separation distance is simply proved to be $7D$. Finally, the influence of WT1 wake on WT2 is discussed.

5.1. Numerical Model

For the two wind turbines, the length of the wake flow field should be longer and thus more computational time is needed. For this, the size of the computation domain is extended to 2772 m × 1260 m × 468 m. The details can be seen in Figure 18. The mesh refinement is the same as that shown in Section 4.1. The size of the outer mesh is 24 m and the inner zone grid size is 3 m.

Moreover, the refined mesh in domain B is also similar to A. The total number of the cell is 4,722,712. The parameters of calculation are similar to those in Section 4.1. According to the conclusion above, the wind speed is set as 8 m/s and the tip loss model is changed into the Shen model. It is vital to observe the wake that is fully developed, so the simulation is calculated for 40 revolutions of WT1, which is around 262 s. Due to the lengthy time of simulation, the time step should be much bigger. The mesh independence tests have been presented previously in Section 4.2.

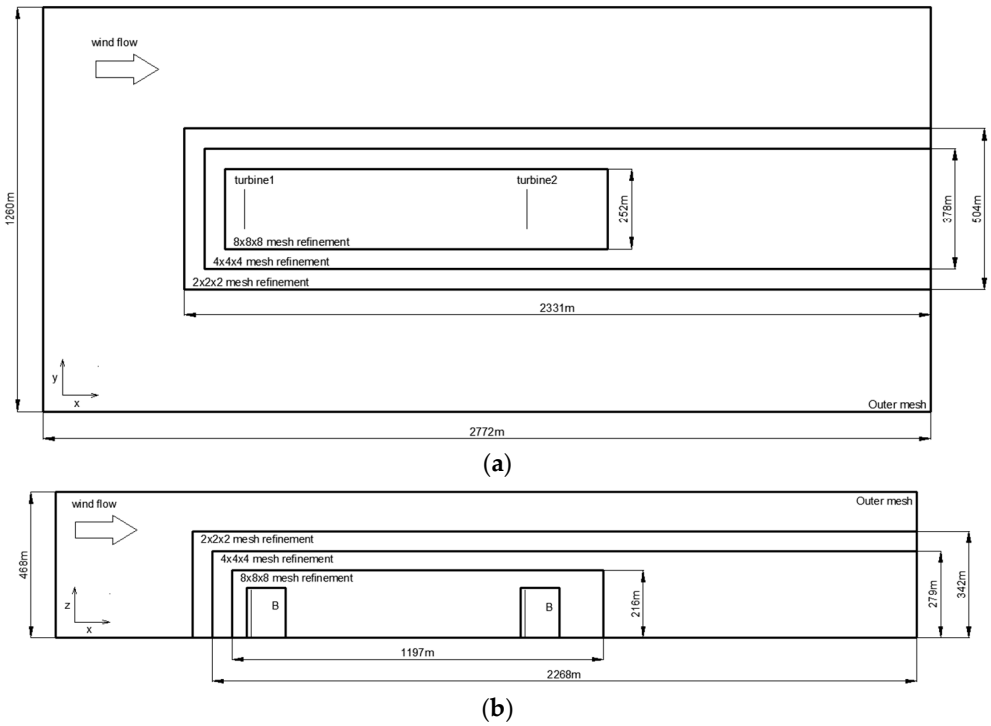

Figure 18. Schematic setup of two wind turbines domain: (**a**) Top view; (**b**) Side view.

5.2. Effect of Different WT2 Tip Speed Ratio

Under the wind speed of 8 m/s, the tip speed ratio of WT1 is 7.55, but this is not true for WT2 because of the WT1 wake. Figure 19 depicts the situation of the power coefficient with different tip speed ratios of WT2. The power coefficient of WT1 shows almost no changes. However, the output power of WT2 varies a lot, and there is a distinct maximum in the range from 6.0 to 6.5. In one word, the tip speed ratio of WT2 is set as 6.1, and details of the power coefficient with different tip speed ratios are shown in Table 10.

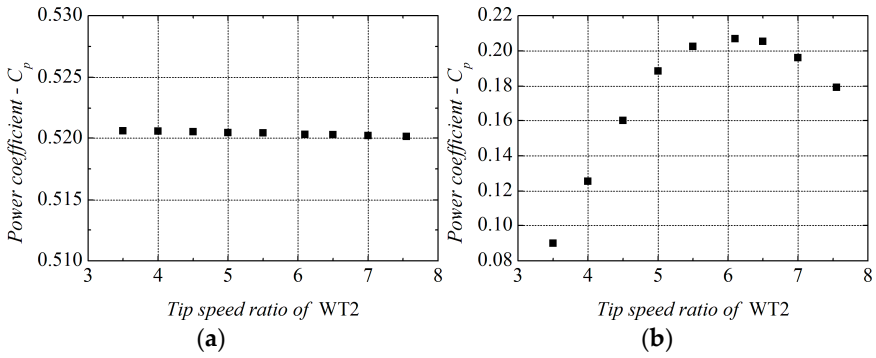

Figure 19. Power coefficient with different tip speed ratio of WT2: (**a**) Power coefficient of WT1; (**b**) Power coefficient of WT2.

Table 10. Power coefficient with different tip speed ratios of WT2.

Tip Speed Ratio of WT2	Power Coefficient (WT1)	Power Coefficient (WT2)
3.5	0.5206	0.0899
4.0	0.5205	0.1256
4.5	0.5205	0.1599
5.0	0.5204	0.1885
5.5	0.5204	0.2024
6.1	0.5203	0.2069
6.5	0.5203	0.2054
7.0	0.5202	0.1961
7.55	0.5201	0.1794

5.3. Effect of Separation

In many studies, the separation of two wind turbines is usually defined $7D$ as a default. From Section 4.4, it could be found that the separation distance should be $6D$, $7D$, or even $8D$. In addition, here, a parameter is set to represent the ability of production in the whole wind farm as:

$$ap = \frac{P}{d} \tag{31}$$

where P is the power of a single downstream wind turbine and d is the average distance between the two wind turbines. The wind speed is assumed to be a constant and this is also true for the production of the downstream wind turbine. Table 11 gives the influence for the distance from $6D$ to $8D$ on the power production. It can be seen that the mean power of WT1 is almost the same, which means that the power of the upstream wind turbine is not influenced by the downstream one. Additionally, the ability of power production has little difference in either the $7D$ or $8D$ case. It is worthwhile to note that the cost of the power transmission is expensive and the loss of electricity transportation is large with the distance. Hence, this distance should be as short as possible and $7D$ is chosen as the realistic value.

Table 11. The mean power and *ap* with different turbine separations.

Mean Power (MW)	Turbine 1	Turbine 2	*ap* (W/m)
6D	2.0312	0.6817	901.7270
7D	2.0345	0.8089	917.1647
8D	2.0336	0.9275	920.1591

5.4. Result of 7D Separation

Although changing the tip loss model from Glauert to Shen and other adjustments make the errors of the mean power larger, it is still with the acceptable range. The comparison of the power with improved ALM by Jha et al. [32] is presented in Table 12, in which the power of WT2 reduces a lot and is only 39.8% of WT1 due to the influence of the WT1 wake effect.

Table 12. The comparison of mean power computed by improved ALM. ALM: Actuator Line Model.

Mean Power (MW)	Turbine 1	Turbine 2
Jha	1.9217	0.8644
turbinesFoam	2.0345	0.8089
Error (%)	5.87	6.42

The power and thrust coefficients of WT1 and WT2 are described in Figures 20 and 21. The tendency of the WT1 power and thrust curves shows almost no changes. Though the curves of WT2 continue to become lower, the reduction is no more than 2%. Besides, the interval between the two extremum points

in WT2 is bigger than WT1. The reason for this is due to the fact that the rotational speed of WT2 is smaller than that of WT1. As can be seen in Figures 20 and 21, the curves between the two extremum points fluctuate significantly. It proves that the WT2 is located in the wake flow field of WT1 and subjected to the flow unsteadiness.

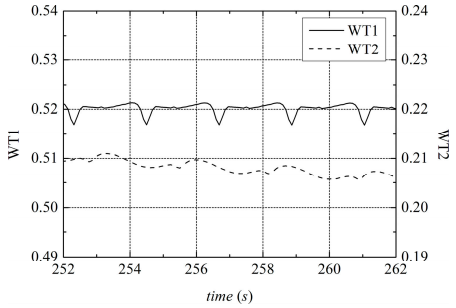

Figure 20. Comparison of power coefficient between WT1 and WT2.

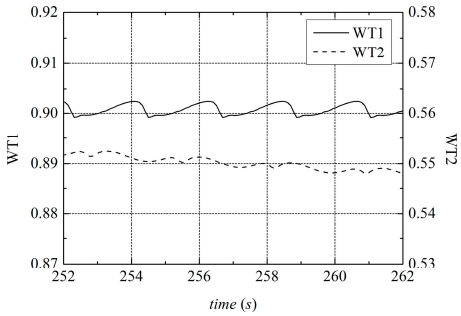

Figure 21. Comparison of thrust coefficient between WT1 and WT2.

Figure 22 shows the radial distributions of average tangential and normal forces of WT1 and WT2. The distribution patterns of WT2 are very similar to those of WT1, and the force amplitude of WT2 is nearly 56% of WT1. It is noted that Figure 22 shows the averaged value of the time but not the instantaneous one, which may not be sufficient to establish a sound conclusion. Considering this, five-points data on the blade are picked up in different times, and their standard deviations are calculated. The outcomes are shown in Figure 23. It can be observed that the standard deviations of WT2 are greater than those of WT1, especially in the case of normal force. This is an indication that the force varies widely, and the forces get their maximums from r/R = 0.6 to r/R = 0.8. Consequently, the loading distribution of WT2 is lower than that of WT1 across the range.

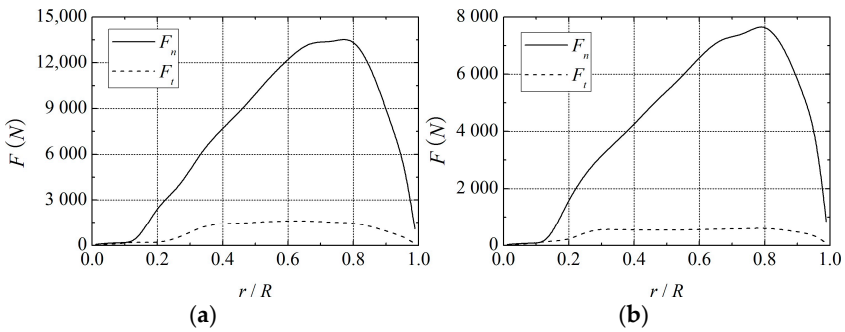

Figure 22. Tangential and normal force distribution in radial direction: (**a**) WT1; (**b**) WT2.

According to the discussion above, the distribution of the forces on the blades and the stabilization of the force both affect the production of the wind turbine. Because of the power of WT1 being higher, the stabilization effect is more crucial than the distribution one. Besides, the distribution is more highly concentrated and the range of change is larger in the middle of the blades, where the blades are easily damaged and need to be paid much more attention during the design.

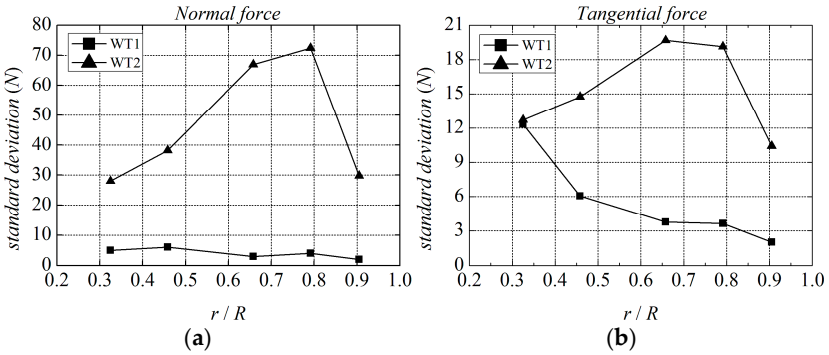

Figure 23. Standard deviations of the normal and tangential force. (**a**) Normal force; (**b**) Tangential force.

Furthermore, Figure 24 depicts the radial distributions of averaged axial flow interference factors. It can be seen that the WT1 distribution of a is similar to that in Section 4.3. The tendency of a is almost the same between WT1 and WT2, but the value is much bigger in WT2. This means that the performance of WT2 is worse than that of WT1, in spite of the fact that the distribution of force on the blades is similar.

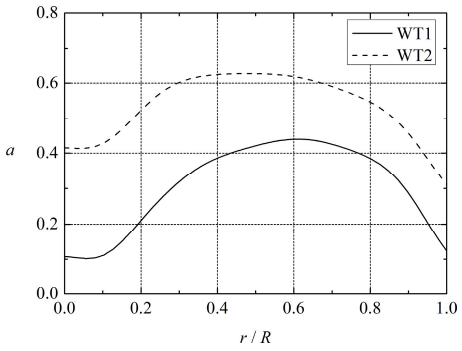

Figure 24. Radial distributions of averaged axial flow interference factors.

To disclose the primary trends of wake-to-wake velocity effect and study the ability of the wind turbine to extract useful momentum from the incoming flow, it is important to analyze the velocity profiles in the wake. The distribution of the mean axial velocity ratio at the hub height is given in Figure 25. From the figure, there are two pronounced velocity deficits, and the first maximum velocity deficit is bigger than the second one. That caused the quantities of momentum extraction by the rotor of WT1 from the incoming wind to be higher and thus its power is larger. From 2D to 6D, the velocity ratio increased by 0.2, and it grew nearly 0.25 from 10D to 14D. Thus, the velocities recovered much faster behind WT2 rather than WT1. This phenomenon may be supposed to be related to the structure of the complex overlapped vortices. After 14D, the rate of velocity recovery is then slower, but the velocity is below 8 m/s, and this should be caused by the arrival upstream wake combined with the wake of WT2.

Finally, to evaluate the effects of the velocity recovery in the wake region, the spanwise distributions of the average axial normalized velocity at different locations are shown in Figure 26. Before 5D, the distribution of velocity in the wake flow field is similar to that found in Section 4.4, where the distinct velocity deficit can be observed and the velocity profiles change from a double peak

into a single peak. After the wind flow passing through WT2, there is another velocity deficit, which is more serious than before. From 8*D* to 10*D*, the magnitude of the velocity deficit is approximately 0.3, but it is only about 0.15 from 1*D* to 3*D*. That quantitatively proves that the level of the velocity recovery behind WT2 is higher again. At the region after 11*D*, the velocity recovers only a little and the value of the velocity ratio is not in unity. That is mainly due to the overlap of the upstream wake from WT1 and the wake generated by WT2.

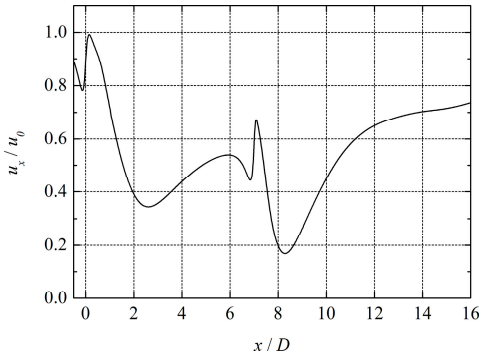

Figure 25. Distributions of the average axial velocity at hub height.

Overall, the existence of WT2 has no influence on the performance of WT1. As a result, it can be concluded that only the upstream wind turbine can work at the designed status, and the downstream wind turbine cannot achieve this due to the influence of the wake, which has been generated by either a single or multiple upstream wind turbines. Due to the effect of the wake generated by the upstream wind turbine, the loading on the blades of the downstream one is more unsteady and as a result, its fatigue damage deserves further study.

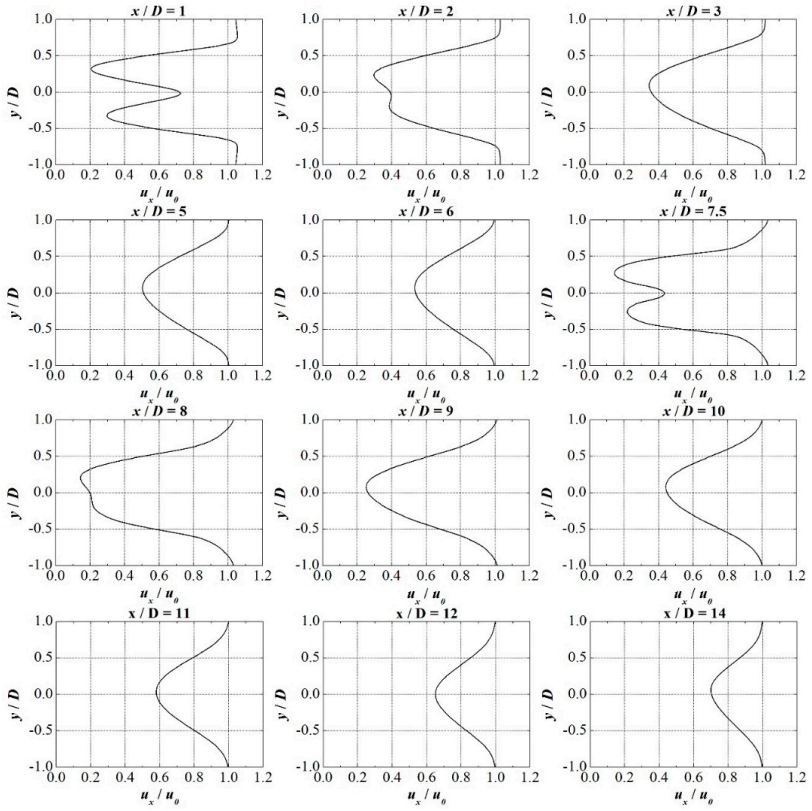

Figure 26. Spanwise profile of average axial velocity at different locations.

6. Conclusions and Discussions

The purpose of the present research is to investigate the harmful effect caused by the wake flow, so a single wind turbine and double wind turbines aligned in a line are modeled using ALM. The major results are summarized as follows:

1. It is reasonable to set the wind speed as 8 m/s. The NREL 5-MW wind turbine could obtain a better working status at this speed, the damage to the blades is minimal, and its wake recovery is fast.
2. It is proved through the velocity deficit that the separation distance of two turbines should not be less than 5*D*, because of the great influence of the wake. This conclusion is the same as that found by Choi et al. [33]. A more in-depth investigation found that the best separation is nearly 7*D*.
3. The upstream wind turbine has a great effect on the downstream one. Due to the wake generated by the upstream wind turbine, the output power and the loading of the downstream one are heavily influenced.

ALM is used in the model, and the result is shown to be accurate enough, but some limitations exist. For example, the elasticity of the blades is not considered adequately and added into the fully coupled system of the floating offshore wind turbine. Further study is required to refine the model and make it more widely acceptable.

Acknowledgments: This work is supported by the National Natural Science Foundation of China (Nos. 51739001, 51579056 and 51279041), Foundational Research Funds for the Central Universities (Nos. HEUCDZ1202, HEUCF170104), Defense Pre Research Funds Program (No. 9140A14020712CB01158), and Open fund of the State Key Laboratory of coastal and offshore engineering of Dalian University of Technology (LP1707) to which the authors are most grateful. Qingwei Ma also thanks the Chang Jiang Visiting Chair Professorship scheme of the Chinese Ministry of Education, hosted by HEU.

Author Contributions: Ziying Yu made the computations, conducted data analysis, and wrote this paper; Xing Zheng did the proof reading; Qingwei Ma guided the whole project.

Conflicts of Interest: The authors declare no conflict of interest.

References

1. Gaumond, M.; Réthoré, P.-E.; Ott, S.; Peña, A.; Bechmann, A.; Hansen, K.S. Evaluation of the wind direction uncertainty and its impact on wake modeling at the Horns Rev offshore wind farm. *Wind Energy* **2014**, *17*, 1169–1178. [CrossRef]
2. Thomsen, K.; Sørensen, P. Fatigue loads for wind turbines operating in wakes. *J. Wind Eng. Ind. Aerodyn.* **1999**, *80*, 121–136. [CrossRef]
3. Vermeer, L.J.; Sørensen, J.N.; Crespo, A. Wind turbine wake aerodynamics. *Prog. Aerosp. Sci.* **2003**, *39*, 467–510. [CrossRef]
4. Betz, A. Das Maximum der Theoretisch Möglichen Ausnützung des Windes durch Windmotoren. *Z. Gesamte Turbinewesen* **1920**, *26*, 307–309.
5. Glauert, H. Airplane Propellers. In *Aerodynamic Theory*; Durand, W.F., Ed.; Springer: Berlin/Heidelberg, Germany, 1935; Volume 3, pp. 191–200. ISBN 978-3-642-91487-4.
6. Tran, T.T.; Ryu, G.J.; Kim, Y.H.; Kim, D.H. CFD-based design load analysis of 5MW offshore wind turbine. In Proceedings of the AIP Conference, Vienna, Austria, 10–14 July 2012; Volume 1493, pp. 533–545.
7. Sanderse, B.; van der Pijl, S.P.; Koren, B. Review of computational fluid dynamics for wind turbine wake aerodynamics. *Wind Energy* **2011**, *14*, 799–819. [CrossRef]
8. Liu, Y.C.; Xiao, Q.; Incecik, A.; Peyrard, C.; Wan, D.C. Establishing a fully coupled CFD analysis tool for floating offshore wind turbines. *Renew. Energy* **2017**, *112*, 280–301. [CrossRef]
9. Castellani, F.; Vignaroli, A. An application of the actuator disc model for wind turbine wakes calculations. *Appl. Energy* **2013**, *101*, 432–440. [CrossRef]

10. Sørensen, J.N.; Shen, W.Z. Numerical modeling of wind turbine wakes. *J. Fluids Eng.* **2002**, *124*, 393–399. [CrossRef]
11. Sibuet Watters, C.; Breton, S.P.; Masson, C. Application of the actuator surface concept to wind turbine rotor aerodynamics. *Wind Energy* **2010**, *13*, 433–447. [CrossRef]
12. Troldborg, N. Actuator Line Modelling of Wind Turbine Wakes. Ph.D. Thesis, Technical University of Denmark, Copenhagen, Denmark, 2009.
13. Meng, H.; Lien, F.-S.; Li, L. Elastic actuator line modelling for wake-induced fatigue analysis of horizontal axis wind turbine blade. *Renew. Energy* **2018**, *116*, 423–437. [CrossRef]
14. NWTC Design Codes (SOWFA). 2003. Available online: http://wind.nrel.gov/designcodes/simulators/SOWFA (accessed on 20 July 2017).
15. The Open Source CFD Toolbox. 2013. Available online: http://www.openfoam.com/ (accessed on 5 May 2017).
16. Churchfield, M.J.; Lee, S.; Michalakes, J.; Moriarty, P.J. A numerical study of the effects of atmospheric and wake turbulence on wind turbine dynamics. *J. Turbul.* **2012**, *13*, 1–32. [CrossRef]
17. Fleming, P.; Gebraad, M.O.; Lee, S.; van Wingerden, J.W.; Johnson, K.; Churchfield, M.; Michalakes, J.; Spalart, P.; Moriarty, P. Evaluating techniques for redirecting turbine wake using SOWFA. In Proceedings of the ICOWES2013 Conference, Lyngby, Denmark, 17–19 June 2013.
18. Fleming, P.; Gebraad, M.O.; Lee, S.; van Wingerden, J.W.; Johnson, K.; Churchfield, M.; Michalakes, J.; Spalart, P.; Moriarty, P. Simulation comparison of wake mitigation control strategies for a two-turbine case. *Wind Energy* **2015**, *18*, 2135–2143. [CrossRef]
19. TurbinesFoam. 2014. Available online: https://github.com/turbinesFoam (accessed on 20 July 2017).
20. Shen, W.Z.; Mikkelsen, R.; Sørensen, J.N. Tip Loss Corrections for Wind Turbine Computations. *Wind Energy* **2005**, *8*, 457–475. [CrossRef]
21. Jonkman, J.; Butterfield, S.; Musial, W.; Scott, G. *Definition of a 5-MW Reference Wind Turbine for Offshore System Development*; National Renewable Energy Laboratory: Lakewood, CO, USA, 2009.
22. Zheng, X.; Ma, Q.W.; Duan, W.Y. Incompressible SPH method based on Rankine source solution for violent water wave simulation. *J. Comput. Phys.* **2014**, *276*, 291–314. [CrossRef]
23. Vinokur, M. On one-dimensional stretching functions for finite-difference calculations. *J. Comput. Phys.* **1983**, *50*, 215–234. [CrossRef]
24. Roache, P.J. Systematic Grid Convergence Studies and the Grid Convergence Index (GCI). In *Verification and Validation in Computational Science and Engineering*; Roache, P.J., Ed.; Hermosa publishers: Albuquerque, NM, USA, 1998; pp. 255–267, ISBN 9780913478080.
25. Celik, I.B.; Ghia, U.; Roache, P.J.; Freitas, C.J.; Coleman, H.W.; Raad, P.E. Procedure for Estimation and Reporting of Uncertainty Due to Discretization in CFD Applications. *ASME J. Fluids Eng.* **2008**, *130*. [CrossRef]
26. Cosner, R.R.; Oberkampf, W.L.; Rumsey, C.L.; Rahaim, C.P.; Shih, T.P. AIAA Committee on Standards for Computational Fluid Dynamics: Status and Plans. In Proceedings of the 44th Aerospace Sciences Meeting and Exhibit, Reno, NV, USA, 9–12 January 2006.
27. Xing, T.; Stern, F. Factors of safety for Richardson extrapolation. *J. Fluids Eng.* **2010**, *132*. [CrossRef]
28. Eça, L.; Hoekstra, M. An uncertainty estimation exercise with the finite-difference and finite-volume versions of parnassos. In Proceedings of the Workshop on CFD Uncertainty Analysis, Lisbon, Portugal, 21–22 October 2004.
29. Ladson, C.L. *Effects of Independent Variation of Mach and Reynolds Numbers on the Low-Speed Aerodynamic Characteristics of the Naca 0012 Airfoil Section*; NASA Scientific and Technical Information Division: Washington, DC, USA, 1988.
30. McCroskey, W.J. *A Critical Assessment of Wind Tunnel Results for the Naca 0012 Airfoil*; No. NASA-A-87321; NASA Mofett field Research Center: Washington, DC, USA, 1987.
31. Mo, J.O.; Choudhry, A.; Arjomandi, M.; Kelso, R.; Lee, Y.H. Effects of wind speed changes on wake instability of a wind turbine in a virtual wind tunnel using large eddy simulation. *J. Wind Eng. Ind. Aerodyn.* **2013**, *117*, 38–56. [CrossRef]

32. Jha, P.K.; Churchfield, M.J.; Moriarty, P.J.; Schmitz, S. The effect of various actuator-line modeling approaches on turbine-turbine interactions and wake-turbulence statistics in Atmospheric Boundary-Layer Flow. In Proceedings of the 32nd ASME Wind Energy Symposium, National Harbor, MD, USA, 13–17 January 2014.
33. Choi, N.J.; Nam, S.H.; Jeong, J.H.; Kim, K.C. Numerical study on the horizontal axis turbines arrangement in a wind farm: Effect of separation distance on the turbine aerodynamic power output. *J. Wind Eng. Ind. Aerodyn.* **2013**, *117*, 11–17. [CrossRef]